



**PATENT**

**IN THE UNITED STATES PATENT AND TRADEMARK OFFICE**

Application No.: 10/663,310

Filing Date: September 16, 2003

Applicant: Mau-Song Chou et al.

Group Art Unit: 2878

Examiner: Otilia Gabor

Title: DETECTION AND ANALYSIS OF CHEMICAL AND  
BIOLOGICAL MATERIALS BY PASSIVE EMISSION OF  
TERAHERTZ WAVE AGAINST A COLD BACKGROUND  
TARGET

Attorney Docket: NGC-00088 (339-804)

---

Mail Stop Appeal Brief - Patents  
Commissioner for Patents  
P.O. Box 1450  
Alexandria, VA 22313-1450

**APPELLANT'S REPLY BRIEF**

Sir:

This is Appellant's Reply Brief pursuant to 37 CFR 41.41 in response to the Examiner's Answer mailed March 13, 2006.

From the Argument section of the Examiner's Answer, it appears that the Examiner is relying solely on the language "sub-millimeter spectroscopy" to provide a motivation to combine the Luukanen imaging system with the systems taught by Laufer, Chou or Butler. The Examiner states that sub-millimeter spectroscopy inherently includes a generation of an emissions spectrum from the object under scrutiny.

BEST AVAILABLE COPY

Appellant respectfully submits that sub-millimeter spectroscopy does not inherently refer to emissions spectrum spectroscopy, but can include other types of spectroscopy, including imaging spectroscopy and absorption spectroscopy.

Further, the language relied on by the Examiner in column 12, lines 43-48 of Luukanen states that the system of the invention can be used not only for searching weapons and smuggled goods, but also for sub-millimeter-range spectroscopy. As Appellant has argued throughout the prosecution of this application, Luukanen only teaches an imaging system. This is clear because Luukanen only discloses detectors that provide imaging, such as antenna coupled bolometers, and not spectrometers. Therefore, Appellant submits that "the system of the invention" is an imaging system.

Appellant refers the Board to the Abstract of Luukanen where it states "[t]he invention relates to detection performed over millimeter and sub-millimeter wavelengths, especially to imaging solutions functioning over a sub-millimeter-wavelength range. The system of the invention uses detectors, comprising antenna coupled bolometers together with wavelength selective optics." Appellant respectfully submits that Luukanen specifically states that their sub-millimeter wavelength system is an imaging system.

To support Appellant's position that sub-millimeter wave radiation can be used for imaging, Appellant hereby provides the chapter on Terahertz Imaging from Mittleman, D., "Sensing with Terahertz Radiation". Appellant submits that sub-millimeter waves are in the terahertz frequency range. Section 3 in the Terahertz Imaging chapter of this book specifically states that "numerous examples of sub-millimeter and millimeter-wave imaging can be found in the literature." Appellant

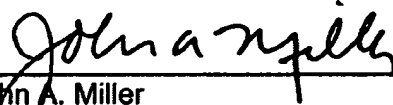
submits that when Luukanen refers to sub-millimeter spectroscopy, he is only referring to sub-millimeter spectroscopy for imaging purposes.

Appellant respectfully submits that there is no teaching in Luukanen et al., or any other reference of record, of providing a cold background in the field-of-view of a sample that is being analyzed using emissions spectroscopy.

For the reasons given above and in Appellant's Brief, it is respectfully requested that the Examiner's rejection under §103 be reversed.

Respectfully submitted,  
**WARN, HOFFMANN, MILLER  
& LaLONE, P.C.**  
Attorneys for Applicant(s)

Date: 5/15/06

  
\_\_\_\_\_  
John A. Miller  
Registration No. 34,985

P.O. Box 70098  
Rochester Hills, MI 48307  
Telephone: (248) 364-4300  
Facsimile: (248) 364-4285

D. Mittleman

(Ed.)

# Sensing with Terahertz Radiation



Springer

Professor Daniel Mittleman  
Rice University  
Electrical and Computer Engineering Department MS-366  
6100 Main Street  
Houston, TX 77005  
USA  
E-mail: daniel@rice.edu

ISSN 0342-4111

ISBN 3-540-43110-1 Springer-Verlag Berlin Heidelberg New York

Cataloging-in-Publication Data applied for

Bibliographic information published by Die Deutsche Bibliothek

Die Deutsche Bibliothek lists this publication in the Deutsche Nationalbibliothek;  
detailed bibliographic data is available in the Internet at <<http://dnb.ddb.de>>.

This work is subject to copyright. All rights are reserved, whether the whole or part of the material is concerned, specifically the rights of translation, reprinting, reuse of illustrations, recitation, broadcasting, reproduction on microfilm or in any other way, and storage in data banks. Duplication of this publication or parts thereof is permitted only under the provisions of the German Copyright Law of September 9, 1965, in its current version, and permission for use must always be obtained from Springer-Verlag. Violations are liable for prosecution under the German Copyright Law.

Springer-Verlag Berlin Heidelberg New York  
a member of BertelsmannSpringer Science+Business Media GmbH

<http://www.springer.de>

© Springer-Verlag Berlin Heidelberg 2003

Printed in Germany

The use of general descriptive names, registered names, trademarks, etc. in this publication does not imply, even in the absence of a specific statement, that such names are exempt from the relevant protective laws and regulations and therefore free for general use.

Data conversion by EDV-Beratung F. Herweg, Hirschberg

Cover concept by Studio Calamar Stenzen using a background picture from The Optics Project, Courtesy of John T. Foley, Professor, Department of Physics and Astronomy, Mississippi State University, USA.

Cover production: design & production GmbH, Heidelberg

Printed on acid-free paper SPTN 10780709 56/3141/dl 5 4 3 2 1 0

# Terahertz Imaging

Daniel Mittleman

## 1 Introduction

Recent years have seen a resurgence of interest in the science and technology of far-infrared radiation. A wide range of new techniques for the generation and detection of far-IR light have been proposed and demonstrated, many of which have relied on nonlinear optical techniques. Although the use of nonlinear optics for far-infrared generation was proposed as early as 1976 [1], widespread application has been hindered until recently by the limited availability of suitable laser sources. With the rapid advances in laser technology, the use of techniques such as optical rectification and difference frequency generation for the production of far-infrared radiation have proliferated. One of the earliest and most promising of these techniques is terahertz time-domain spectroscopy (THz-TDS), a method which relies on the generation of broadband electromagnetic transients using ultrafast laser pulses. This method, pioneered in the late 1980s by groups at AT&T Bell Laboratories [2] and IBM's T. J. Watson Research Center [3], has become increasingly popular with the widespread availability of femtosecond laser sources. Because of the challenges associated with more conventional methods of far-infrared research, this novel THz source has proven to be quite valuable for spectroscopy. Further, the ultrashort duration of the THz pulses, the associated broad bandwidth, and the fact that these pulses are inherently synchronized with a femtosecond pulse train have enabled several novel measurement techniques, which would otherwise be impractical. Examples include time-resolved techniques such as the optical pump, THz probe measurement, THz emission spectroscopy, and correlation spectroscopy. Nuss and Orenstein have recently reviewed the application of THz-TDS to the study of solid-state systems; this work contains numerous examples of both linear spectroscopy and these other techniques [4]. THz-TDS has also been used to study gases, most notably by Grischkowsky and coworkers [5-11].

In 1995, Hu and Nuss reported the first use of THz-TDS for imaging [12]. This work has sparked a flood of interest in the field and in the public media [13], as it immediately suggested a range of new and interesting applications for this spectrometer. The ability to form images in a reasonable time, combined with the unique properties of THz radiation, has inspired an amazing array of suggested applications areas, ranging from biomedical diagnosis to

the monitoring of the water content of packaged food products and to fault detection in packaged integrated circuits. In this chapter, we review the rapid developments in THz "T-ray" imaging which have occurred since the initial report. We describe a number of different examples, which illustrate the capabilities and limitations of this novel imaging technique. This chapter does not seek to provide a tutorial on how to construct a THz imaging system; numerous different system configurations have been employed, and an exhaustive review of these is beyond the scope of this chapter. We provide a description of a typical system, highlighting those features which are important for the various imaging modes discussed later. The reader is referred to a number of reviews on this subject for more information [4, 14-16]. We note that focal-plane imaging using free-space electro-optic sampling has also been demonstrated [17]. This technique is related to the methods described here, and is discussed in the chapter by Jiang and Zhang in this volume.

## 2 Key Components of a THz Imaging System

Figure 1 is a schematic diagram of a typical THz-TDS spectrometer used for T-ray transmission imaging. The spectrometer consists of a femtosecond laser, a computer-controlled optical delay line, an optically gated THz transmitter, optics for collimating and focusing the THz beam, the sample to be imaged, an optically gated THz receiver, a current preamplifier, and a digital signal processor (DSP) controlled by a personal computer. The gross features of this setup have not altered substantially since the initial report of the first THz-TDS system in 1989 [3]. However, there have been a number of significant advances, which have enabled the imaging applications. Several of these, including the use of a rapid scanning optical delay line and DSP data acquisition, were first noted by Hu and Nuss [12]. Others, such as the

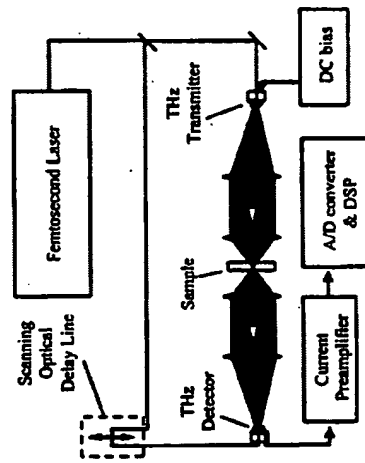


Fig. 1. Schematic of a terahertz time-domain spectrometer used for transmission imaging. The sample is located at an intermediate focal plane, and can be scanned in the two transverse dimensions for image formation

use of structured electrodes on the THz emitter and detector antennas, were described later [18,19]. Here, a brief comment on the state of the art of each component is presented.

### 2.1 The Femtosecond Laser Source

The vast majority of the work in this field has been carried out using mode-locked Ti:sapphire lasers, operating near a wavelength of 800 nm. These are the most widespread femtosecond laser sources, and the laser parameters (pulse duration, wavelength, and output power) are all ideally suited for driving GaAs-based THz emitters and detectors, as well as radiation-damaged silicon-on-sapphire (rd-SOS). These lasers typically provide excellent pulsed-to-pulse and long-term stability, and are relatively easy to operate. Indeed, the first commercialized version of the THz-TDS system, announced in January 2000, is based on Ti:sapphire technology [20].

Despite this impressive level of success, the possibility of employing different femtosecond laser sources is of interest, for several reasons. First, although the noise performance of typical Ti:sapphire laser systems is quite good compared with most other femtosecond sources, it can be the limiting factor in the noise in THz waveform measurements. Second, these lasers are usually quite sensitive to small changes in optical alignment, and are thus not stable against mechanical vibrations. In order to construct a portable THz imaging system, a more robust femtosecond laser is desired. An excellent alternative is the mode-locked fiber laser, in which the light pulses propagate entirely within an optical fiber. Such lasers are commercially available, and a considerable amount of research is being directed towards the development of THz emitter and receiver antennas which can operate when driven at  $\sim 1550$  nm, the wavelength of these fiber sources. One can no longer use GaAs, since this wavelength is below the band gap of the material. Other candidate materials include GaAs-based ternary and quaternary alloys [21,22], InAs [23], and ion-implanted germanium [24].

### 2.2 Optical Delay Line

The THz-TDS system requires a means for varying the delay of one optical beam relative to a second, in order to move the sampling gate across the waveform to be sampled. In nearly all cases, this is accomplished by varying the optical path length traversed by one of the beams. Often, the alignment of the optical beam onto the detector is more sensitive than the alignment of the generating beam, although this depends on the details of the antenna structures employed. In these cases, it makes more sense to place the variable delay in the generating arm. This optical delay is typically generated using a retroreflecting mirror arrangement mounted on a mechanical scanner. This can either be a slow stepper motor or a rapidly oscillating device such as

a galvanometer. The speed of the scanner dictates the arrangement for the data acquisition, as described below.

In many imaging applications, it is desirable to scan the optical delay as rapidly as possible. In order to increase the waveform acquisition rate. There are a number of difficulties associated with this; one problem is that there are not many mechanical delay lines which can provide a sufficient delay window at higher than a few tens of hertz. To obtain a window of 100 ps, the retroreflecting mirror arrangement must oscillate with an amplitude of  $\sim 1.5$  cm. Ideally with a displacement which varies linearly with time over as much of this window as possible. This is difficult to achieve using mechanical shakers; one device which has been commonly employed, manufactured by Clark MXR, Inc., has a mechanical resonance near 20 Hz, and cannot be driven safely beyond  $\sim 100$  Hz. For this reason, the majority of the point-by-point THz images taken to date have been acquired at a rate of 20 pixels per second, which translates to a few minutes per image. For certain applications, a much smaller delay window (e.g. a few picoseconds) is sufficient, in which case much higher waveform acquisition rates can be obtained by mounting a mirror on a piezoelectric transducer. Numerous other methods for varying the timing of the two pulse trains have been proposed, although none are yet in widespread use in THz systems.

### 2.3 Terahertz Optoelectronic Switches

While the THz transmitter and receiver designs were identical in early THz-TDS work, a wide range of different structures have been investigated, and optimized either for maximum signal or maximum bandwidth. Grischkowsky and coworkers pioneered the coplanar strip line for use as a THz emitter [25]. This structure is appealing both for the simplicity of the design and for the extremely broadband emission which can be produced. Using 60 fs pulses, spectral coverage to 6 THz can be achieved [26].

For many of the imaging applications explored to date, more complex structures have been used to produce a larger signal at the expense of the enhanced bandwidth. Figure 2a shows one commonly used design, in which the emitted signal is optimized through the use of a structured electrode [18]. This antenna consists of two 10  $\mu\text{m}$  wide metal lines deposited on semiconducting GaAs, with a separation of 100  $\mu\text{m}$ . Two metal tabs extend out from these lines towards each other; these tabs may terminate in either flat or triangular ends. The gap between the two tabs can be as small as 5  $\mu\text{m}$ , or as large as 100  $\mu\text{m}$ . A voltage is applied across the two lines, creating a strong depletion field near the anode. Focusing a few tens of milliwatts of the femtosecond beam near the corners or points of the anode structure gives rise to a greatly enhanced THz emission, as a result of this enhanced depletion field. Figure 2b shows the enhancement of the emitted THz field, as the laser focus is moved relative to the position of the emitter antenna. Numerous other antenna designs have been employed [19,27].

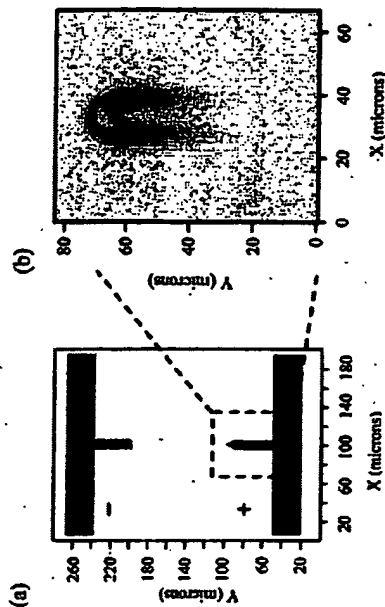


Fig. 2. (a) One commonly used design for high-efficiency THz emitters, with a pointed electrode to enhance the electric field strength. (b) Strength of the peak THz emission as a function of the location of the optical beam spot relative to the pointed electrode. The THz field is most intense when the optical beam is focused at the point [18]. Data supplied courtesy of I. Brener

The most commonly used THz receiver design has been a simple dipole antenna, roughly 50  $\mu\text{m}$  in length [2]. A number of variations on this design have been employed, such as the interdigitated structure shown in Fig. 3. For a Hertzian dipole antenna, with a length much less than the wavelength of the radiation, the collection sensitivity and radiation efficiency both vary inversely with the wavelength. Thus, smaller dipole antennas provide a broader-bandwidth response; dipoles as small as 30  $\mu\text{m}$  have been used. Of course, this  $1/\lambda$  dependence no longer applies when the radiation wavelength in the substrate becomes comparable to the dipole length, so the details of the high-

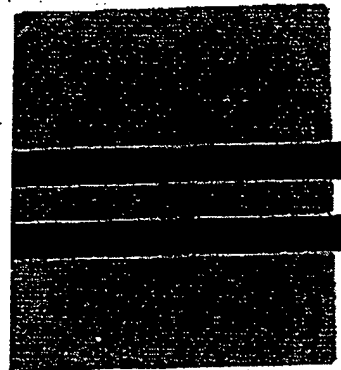


Fig. 3. Photograph of an interdigitated electrode design lithographically deposited on radiation-damaged silicon-on-sapphire, for use as a THz receiver



frequency response are more complex. In addition, the low-frequency roll-off in these quasi-optical systems is typically limited by diffraction effects due to the finite size of optical elements such as the substrate lenses mentioned below. As a consequence, the  $1/\lambda$  dependence may apply over only a rather limited spectral range. A detailed analysis of a THz-TDS system can accurately predict the measured spectral response, as long as all of these effects are taken into account [15].

If very small dipole antennas are used for both transmission and detection, the high-frequency limit is generally determined by the temporal response of the system. One obvious manifestation of this limit is the duration of the laser pulses used to generate the THz radiation. The majority of THz-TDS experiments have employed pulses of  $\sim 100$  fs duration, since these are the easiest to obtain from commercial systems. Such pulses can be used to generate radiation via a number of different mechanisms, including the "current surge" mode, which produces the largest signals, and optical rectification, which provides the broadest bandwidth. Either way, the radiation cannot contain frequency components varying more rapidly than the derivative of the pulse envelope, which limits the bandwidth to  $\sim 4.5$  THz for 100 fs pulses. Consequently, shorter pulses are often used to generate bandwidth extending into the mid-infrared [28-30].

A second important limiting factor is the response time of the photoconductive material used as a substrate for the THz antennas. This limit is most pronounced in the receiver antenna, since one does not expect the highest measured frequency to exceed the inverse of the temporal width of the photo-generated sampling gate. In most cases, this duration is limited by the carrier trapping time, although a number of schemes have been proposed to avoid this limitation [31-32]. As a consequence, the most commonly used materials are those which are characterized by subpicosecond free-carrier lifetimes, as well as strong optical absorption at  $\sim 800$  nm, high carrier mobilities, and low dark currents. The two most common choices are radiation-damaged silicon-on-sapphire [14] and low-temperature-grown GaAs [33]. The former material has been demonstrated to provide an excellent high-frequency response, producing THz pulses shorter than 400 fs [25-34]. The latter provides performance comparable to that of *rel-SOS*, although with somewhat lower bandwidth [35].

It should be noted that it is possible to detect broadband THz radiation even using a photoconductive antenna with a slow carrier lifetime. In this case, one relies not on the width of the sampling gate, but merely on its fast-rising edge. If the photocurrent can be modeled as a step function, then the detector operates as a fast sampling gate in an integrating mode, and the measured signal is proportional to the integral of the incident THz field [31]. In this configuration, the bandwidth is limited by the speed of the rising edge of the current, which is determined by the duration of the optical pulse, and by the *RC* time constant of the antenna. Bandwidths up to 20 THz have

been reported recently, using substrates with carrier lifetimes of more than 1 picosecond [36].

## 2.4 Terahertz Beam Optics

A key ingredient to a high-performance T-ray imaging system is an optical system that (1) allows one to focus the THz waves to a diffraction-limited focal point at the object, and (2) has the highest possible throughput. Unlike optical systems designed for visible light, the wavelength of the THz electromagnetic signals is not negligible compared with the size of the optical elements used, and diffraction effects can dominate ray propagation. This can be a significant complication in the design of optical systems for the THz frequency region. Additionally, because of the large spectral bandwidth, the optical system needs to be achromatic and exhibit a flat phase response over the frequency range of the pulse.

A critical component that enables these features of the THz beam system is the substrate lenses, which are attached to the backs of the transmitter and receiver chips [3]. The substrate lenses improve the coupling of the light into and out of the photoconducting antennas, and suppress the excitation of slab modes. These lenses are generally composed of high-resistivity (greater than  $10^4 \Omega \text{ cm}$ ) silicon, which is dispersionless over the whole THz range [37]; as a result, these lenses exhibit no chromatic aberration.

Two different lens designs are commonly used. The first of these places the transceivers at the focal point of the substrate lens [14,15,38]. With this design, the distance from the transceiver to the tip of the lens is given by  $R[1 + 1/(n-1)]$ , where  $R$  is the radius of the lens and  $n$  is the refractive index of the lens material, assumed to be the same as that of the substrate. With this collimating hyperhemispherical design, rays emitted near the optical axis emerge as a collimated beam. However, light emitted at larger angles emerges at substantial angles, so the lens is astigmatic. At still larger angles, radiation is internally reflected at the lens-air interface, and thus lost. A ray-tracing diagram illustrating these effects is shown in Fig. 4a. Further, the threshold angle of total internal reflection defines an effective aperture size for the lens, which in turn can lead to additional diffraction of the emerging beam.

A second commonly used substrate lens design is the aplanatic hyperhemisphere, for which the transceiver-to-lens-tip distance is  $R(1 + 1/n)$  [4,16]. This arrangement ensures that the critical angle for total internal reflection corresponds to rays emitted at  $90^\circ$ ; that is, parallel to the plane of the substrate. Thus, the light lost to internal reflection is minimized, and simultaneously the effective lens aperture is maximized. It is relatively straightforward to show that, for silicon substrate lenses ( $n = 3.42$ ), the effective aperture is larger using the aplanatic design, by roughly 13%. More significantly, the emerging beam does not exhibit the astigmatism of the collimating design but, rather, diverges as a Gaussian beam with a half-angle of  $\sin^{-1}(1/n)$ . Figure 4b shows a ray diagram for an 8 mm diameter aplanatic silicon hyperhemisphere.

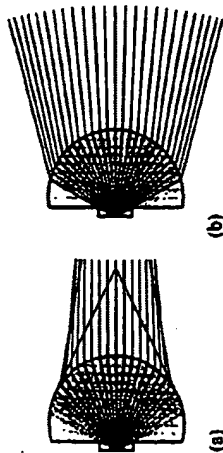


Fig. 4. Ray-tracing diagrams of the two lens designs described in the text. (a) Collimating lens design. The aberration of the wavefront, arising from rays propagating close to the critical angle inside the lens, is evident. The rays represented by dashed lines are those that are trapped inside the lens by total internal reflection. (b) Hyperhemispherical lens design. In which no rays are internally reflected, and the emitted radiation emerges with a divergence half-angle of about  $15^\circ$  and no wavefront aberration. These diagrams are shown to scale for a substrate lens of 4 mm radius, with a refractive index equal to that of silicon,  $n_{\text{Si}} = 3.418$ . In both cases, the antenna is fabricated on a 2 mm square GaAs substrate, also shown. In the hyperhemispherical design, a substrate of this size can interfere with the propagation of radiation at large angles, and may decrease the emission efficiency as a result. The diagrams neglect the small index difference between GaAs and Si.

The implications of the substrate lens design are most important when one is considering the optical system used to collect and manipulate the THz beam [3,15,16]. For example, a common design would be to place a free-space collection lens or off-axis parabola in front of the emitter, to produce a collimated beam. In the case of the collimating substrate lens, the need for this collection lens can only be understood if diffraction is included, since in the ray-optics description this beam is already collimated. Since the beam that reaches the collection lens is strongly perturbed by diffractive effects, the beam after the collection lens has a frequency-dependent transverse spatial profile. Radiation with higher frequencies propagates closer to the optical axis. If this beam is re-imaged using a second free-space lens, the resulting focal spot is frequency-independent, which can be advantageous for such applications as coupling into waveguides, for example [39]. On the other hand, in the case of the aplanatic substrate lens, one might imagine that the beam is less affected by diffraction, since it emerges as a diverging source (see Fig. 4(b)). In this case, the beam after the collection lens has a transverse profile that is independent of frequency [16]. Re-imaging the beam produces a focal spot with a strongly frequency-dependent diameter. This can be exploited to improve resolution in imaging applications [40]. Also, in the ray-optics picture the beam after the collection lens is collimated in one case, but comes to a beam waist quite rapidly in the other. This could have important implications for the design of a THz system, since it would dictate the required separation between the emitter and receiver antennas [14]. However,

when diffraction effects are included, it is no longer clear that this distinction is important.

Rudd and Mittleman have recently undertaken a thorough experimental and computational comparison of these two substrate lens designs [41]. Although both lens designs have been used extensively for many years, it is only relatively recently that direct comparisons have been performed. Several groups have described simulated and experimental results for the parameters of the beam emerging from the lens, as a function of the (cylindrical) extension of the lens beyond hemispherical [42-44]. These results cover cases similar, though not identical, to the two lens designs mentioned above. This work has usually been concerned with the generation or detection of narrowband emission. The situation in which the emitted radiation is broadband, of particular relevance to THz time-domain spectroscopy, has not previously been addressed. As a result, the dramatic influence of the substrate lens design on the achievable bandwidth in a THz-TDS system has not been generally appreciated.

Figure 5 illustrates measured amplitude spectra, as a function of frequency and emission angle, for the two lens designs described above. These measurements represent the p-polarized E-plane emission from the emitter antenna, a  $90^\circ$  bow-tie fabricated on low-temperature-grown GaAs. In these data, the persistence of higher-frequency components at low angles is more noticeable for the collimating lens than for the hyperhemisphere. This can be understood directly from the ray diagram (Fig. 4), which is increasingly valid at higher frequencies. Also, these data illustrate the pronounced interference fringes at larger angles in both cases.

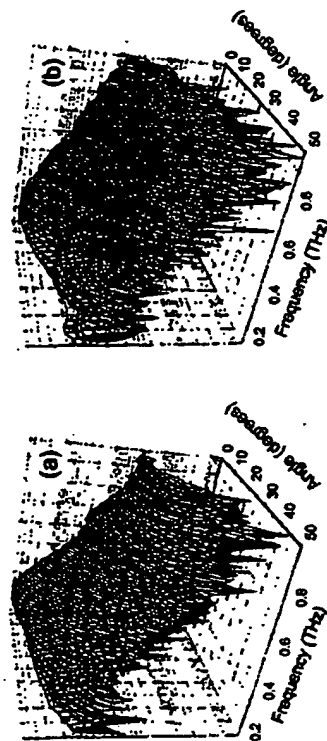


Fig. 5. Amplitude spectra of measured THz waveforms as a function of both frequency and emission angle. (a) E-plane emission from an antenna coupled to a hyperhemispherical lens. (b) E-plane emission from an antenna coupled to a collimating lens. These two plots are shown on common vertical scales, to facilitate comparisons of relative amplitudes. The vertical axes are logarithmic.

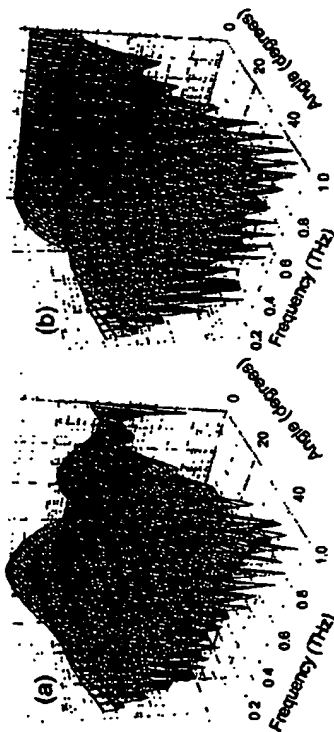


Fig. 8. Simulation of the E-plane emission pattern as a function of both angle and frequency, for (a) the hyperhemispherical lens design and (b) the collimating lens design. These show the amplitude spectra on a logarithmic scale, as in Fig. 5. The hyperhemispherical lens introduces strong interference fringes even at zero degrees, limiting the measurable emission bandwidth of the lens-coupled antenna. In contrast, the collimating design places no such limits on the spectrum, at least within the approximations of the calculation.

Figure 6 shows a calculation which simulates these results. This computation is based on a numerical solution of the Fresnel-Kirchhoff diffraction integral, following the method of Jepsen and Keiding [36]. It is important to note that these calculations do not provide an accurate description of the relative amplitudes of different frequency components within the measured THz wave. These relative amplitudes are determined not only by the interference of the diffracting beam, but also by such factors as the duration of the optical pulses used to gate the antennas, the carrier lifetime in the detector antenna, and the size of the emitter and receiver dipoles [15]. None of these factors are included in these simulations. Nonetheless, it is instructive to see how much of the frequency response is determined solely by the diffraction effects modeled here. It is clear from Fig. 6 that, even in the absence of any other mechanism that could limit the measured THz bandwidth, the geometry of the substrate lens can have a dramatic effect. In the case of the hyperhemispherical lens, the spectral content is limited to  $\sim 0.6$  THz even in the forward direction ( $\theta = 0^\circ$ ), in approximate agreement with the experiment (Fig. 5a). The bandwidth is severely constrained by the geometry of the substrate lens, independent of other limiting factors that are usually considered to be more significant. In contrast, with a collimating lens design, the geometry does not place any limits on the bandwidth along the optic axis, at least up to 1 THz. This highlights an important and usually neglected factor in the optimization of the THz bandwidth for spectroscopic measurements.

Once the radiation has emerged from the substrate lens, a bulk optical system is required to collimate and focus the THz beam in the region where it interacts with the sample to be imaged. This has most often been accomplished using off-axis paraboloidal reflectors, which are broadband and lossless. However, these optics are difficult to align properly, and as a result the THz beam can often exhibit severe spherical aberration. This not only degrades the spatial resolution in an image, but also reduces the measured signal at the detector, since the THz beam spot is distorted. For this reason, transmissive optics have become increasingly popular (see Fig. 1). For signals with less than 2 THz of bandwidth, high-density polyethylene (HDPE) is an excellent choice as an optical material, with very low absorption (less than  $0.04 \text{ cm}^{-1}$  at 300 GHz, rising to  $\sim 1 \text{ cm}^{-1}$  at 2 THz), little dispersion, and small Fresnel reflection losses (a refractive index of 1.52 leads to an insertion loss of order 9% per lens) [45,46]. HDPE exhibits a fairly narrow absorption resonance near 2.2 THz, which can be observed as oscillations following the single-cycle waveform (Fig. 7). For applications in which broad bandwidth is required, high-resistivity silicon lenses may be more appropriate. The disadvantages of silicon optics are the higher Fresnel losses ( $\sim 50\%$  per lens) due to the larger index ( $n = 3.418$  [37]) and the substantially higher cost. In order to alleviate the former difficulty, antireflection coatings may be employed. Several proposals have been made for such coatings [47,48], although no coatings have been reported which are sufficiently broadband to be useful for THz-TDS. A third alternative material is the polyolefine TPX, which has

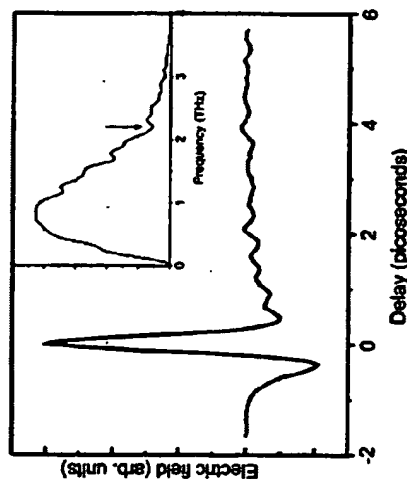


Fig. 7. A waveform measured after propagating through a piece of high-density polyethylene  $\sim 1$  cm thick. The oscillations which follow the initial transient result from the relatively narrow absorption feature in this material at  $\sim 2.2$  THz. This can be observed as a dip in the amplitude spectrum (inset).

the advantage that it is transparent in the visible as well as in the THz range; further, the THz refractive index ( $n = 1.46$ ) is quite similar to the index in the visible region ( $n = 1.43$ ) [45]. This can greatly simplify the alignment of a complex THz optical system, since visible light can be used as a guide. TPX exhibits slightly more absorption than does HDPE at low frequencies, but the spectrum is devoid of features and the power absorption coefficient is still less than  $1 \text{ cm}^{-1}$  even at 3 THz [49].

The propagation of single-cycle THz pulses has been a very active area of research in recent years, in part because of the ease with which these pulses can now be generated and detected. The propagation of radiation pulses with large fractional bandwidths poses an interesting problem in diffractive optics. This problem was first modeled by Ziolkowski and Judkins, shortly after the development of THz-TDS [50], and subsequently explored by a number of groups [15,51–55]. Others have investigated the effects of apertures or waveguides [39,40,56,57]. Substantial reshaping of both the temporal and the spectral profile of the pulse can occur. In most cases, despite the large fractional bandwidths, Gaussian beam models have been sufficient to describe these effects.

## 2.5 Polarization of the THz Beam

As mentioned above, in most cases the emission from THz antennas has been described using the approximation of an ideal dipole [16], producing linearly polarized radiation. Of course, the dipoles used in real THz systems are not ideal, and so the polarization state of the radiation is not, in general, purely linear. The conventional wisdom in the field is that a typical emitter generates a cross-polarized component which is on the order of a few percent as large as the component polarized along the dipole. Cai and co-workers [19] found that the cross-polarized radiation had an amplitude roughly 7% as large as the dominant polarization component, although they provided no explanation for the origin of this small component. Garret et al. [58] reported a frequency-dependent variation in the linear polarization axis, attributed to substrate lens misalignment.

Ruid et al. [59,60] provided the first thorough characterization of the cross-polarized component of the field radiated from a lens-coupled THz antenna, similar to the antenna shown in Fig. 2. For the  $s$ -polarized E-plane emission, the largest peak-to-peak electric field amplitude is approximately 7% of the  $p$ -polarized emission, but this maximum emission occurs at an angle of approximately  $6^\circ$  away from the optical axis. The results are shown in Fig. 8. Figure 8a shows typical  $s$ -polarized waveforms measured at various emission angles, relative to the terahertz-beam optic axis  $\theta = 0$ . Figure 8b summarizes these results for all frequency components, demonstrating a pronounced minimum in the cross-polarized field on the optic axis.

These results have been interpreted as quadrupole, rather than dipole, emission, with the following mechanism [59]. The current flowing into the

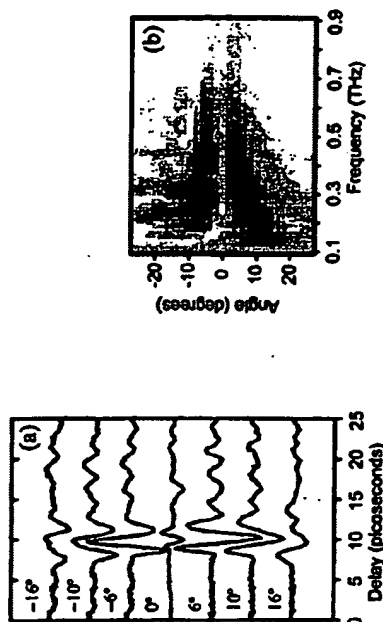


Fig. 8. (a)  $s$ -polarized E-plane waveforms emitted from a structured dipole emitter of the type illustrated in Fig. 2. These cross-polarized THz waveforms are more than an order of magnitude smaller than the component polarized along the dipole axis. Further, the waveforms are largest at angles of  $\pm 6^\circ$  relative to the terahertz-beam optic axis,  $\theta = 0$ . (b) Spectral amplitude of the measured cross-polarized THz radiation as a function of frequency and angle, illustrating the pronounced minimum along the optic axis

dipole is drawn from both ends of the strip-line on one side, and exits the dipole in both directions into the other strip-line. This current distribution is characterized by the length  $L$  of the dipole, and by the distance  $d$  from the dipole to the point at which the current vanishes. This static current distribution possesses zero dipole moment, but a quadrupole tensor with two nonzero elements  $Q_{xx} = Q_{yy} \equiv Q_0$ , where  $Q_0$  is proportional to the product of  $d$  and  $L$ . This quadrupole tensor gives rise to an electric field, which is given by

$$E_Q \propto \sin \theta \cos \theta \sin 2\phi \hat{\theta} + \sin \theta \cos 2\phi \hat{\phi} \quad (1)$$

where  $\phi$  is measured from the axis of the dipole. For E-plane emission ( $\phi = 0$ ),  $E_Q$  is an  $s$ -polarized wave with amplitude  $\sin \theta$ . It should therefore exhibit a null at  $\theta = 0$ , as well as a polarity reversal on either side of  $\theta = 0$ , just as observed in Fig. 8. The angular widths of the emission lobes can be understood in terms of Fresnel diffraction from the exit aperture of the substrate lens [59,60].

## 2.6 Signal Acquisition

The traditional method for acquiring THz waveforms relies on a photoconductive sampling technique. Here, the delay of the generating pulse is swept

relative to that of the detecting pulse, and the average photocurrent generated in the receiver is measured as a function of the delay. The resulting signal is the convolution of the THz waveform with the temporal shape of the photoconductive sampling gate. In order to eliminate the majority of the external noise in these measurements, the signal was usually acquired with a lock-in amplifier, and one of the gating beams (or the THz beam) was modulated with a chopper wheel. Since this required a lock-in time constant in the range of tens to hundreds of milliseconds, the sweep time of the delay was quite slow, on the order of hundreds of milliseconds or more per data point. At this rate, it took several minutes to acquire a single 1024-point THz waveform.

In order to obtain images, where the entire waveform is measured and analyzed at each pixel, this acquisition time must be reduced dramatically. To accomplish this, Hu and Nuss replaced the slow stepper motor with a scanning optical delay line (ODL) [12]. This consists of a small retroreflecting corner cube mounted on a galvanometric shaker. It typically provides up to 100 ps of optical path delay on each sweep, and can sweep at up to 100 Hz. With this device, one directly detects the photocurrent as a function of time, using a synchronized signal from the ODL as a periodic trigger. In most cases, the antenna is connected directly to a current-to-voltage preamplifier, so that a voltage can be observed on an oscilloscope or digitized. Dispersing with the noise filtering provided by the lock-in detection does degrade the signal-to-noise ratio (SNR) somewhat, but allows much faster acquisition times. The amount by which the SNR is diminished depends on the details of the noise sources, but a factor of 100 is not unusual. Nonetheless, a waveform measured with a single sweep of the ODL can typically have an SNR of 1000 or more, which is sufficient for many imaging applications. Figure 9 shows a representative comparison between waveforms acquired using an ODL and lock-in data acquisition.

## 2.7 Data Processing

One of the most important aspects of THz imaging involves the processing of the waveforms acquired at each pixel of the image. Each waveform contains a large amount of information, and the reduction of this to a single, color-coded pixel can be a challenging task. Because of the diversity of samples to be studied and properties to be investigated, the development of a single algorithm for signal processing is impractical. For similar reasons, it makes sense to discuss the processing issues which arise in each particular context individually. The unique set of signal-processing challenges associated with each imaging mode is deferred to the following section, where we provide a number of illustrative examples of images obtained with a THz-TDS system.

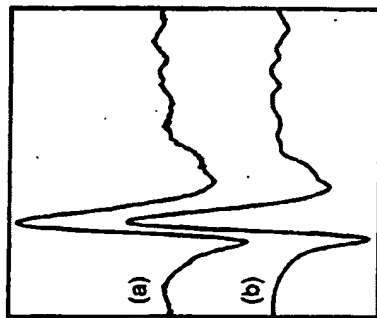


Fig. 9. A comparison of lock-in and ODL data which does not yet exist. (a) THz waveform acquired by averaging multiple sweeps of an optical delay line. (b) The same waveform, acquired using a conventional lock-in amplifier. The two waveforms were acquired with roughly equivalent levels of signal averaging

## 3 Imaging with THz-TDS

Numerous examples of submillimeter- and millimeter-wave imaging can be found in the literature which predate the first demonstration of T-ray imaging [61-63]. In at least one case, an imaging system using an optically pumped methanol laser was installed in a factory for on-line inspection of polyethylene high-voltage cable insulation [64]. However, the practicality of most of these examples for application in "real-world" situations has been limited at best. Even the aforementioned example, although installed in a manufacturing environment, employed an 80 watt CO<sub>2</sub> pump laser, high-speed scanning optics, and liquid-helium-cooled photodetectors, and occupied an entire room [65].

The THz "T-ray" imaging system offers a promising alternative to such cumbersome inspection systems, with a number of advantages. The THz-TDS system can be designed to be compact, efficient, and relatively inexpensive. Unlike the case for many far-infrared systems, no cryogenics are required. In addition, the sub-picosecond duration of the THz pulses and the phase-sensitive detection combine to provide a number of unique imaging modes. This range of advantages has prompted the development of a commercial version of the T-ray system. This device, announced in early 2000 [20], is the first commercially available far-infrared imaging system. In the following paragraphs, we provide several examples of T-ray images, in order to illustrate the unique sensing capabilities of such a system.

### 3.1 Amplitude and Phase Imaging

Once a THz-TDS system with an intermediate focus is constructed (see Fig. 1), one can place an object at this focus and measure the waveform of the THz pulse which has traversed the object. By translating the object, and measuring the transmitted THz waveform for each position of the object, one can build an image pixel by pixel. The image formed in this fashion may represent any desired aspect of the measured waveforms, including amplitude [12,16], phase [15,66], or even combinations of these two [67]. This versatility provides a number of different methods for imaging any given object, each of which can reveal different properties of the sample.

The list of possible applications of such a system is quite extensive. Perhaps the most promising applications lie in the area of quality control of packaged goods. Figure 10 shows a THz image of a  $\sim 2$  cm square portion of a small (1-3/8 oz.) box of cereal. The cardboard box in which the cereal is packaged is nearly transparent to the THz radiation. The dark areas in the image are raisins, which exhibit a high contrast relative to the surrounding material due to their high water content. In this image, the thickness of the sample ( $\sim 5$  cm) is somewhat larger than the confocal parameter of the THz beam ( $\sim 1$  cm); as a result, the raisins (which were not situated at the THz beam focus) appear larger in the image than their actual size. Since one can in principle choose any set of THz beam optics for an imaging system, this effect should not substantially limit the utility of the technique. This imaging tool is well suited for inspection of sealed packages if the packaging is composed of transparent materials such as cardboard, most plastics, thin pieces of dry wood, etc.

Figure 11 illustrates another use of THz imaging as a quality control monitor. This figure shows a THz image of a portion of an automobile dashboard. representative of innumerable mold-fabricated plastic parts. This part consists of two parallel black plastic sheets, with a rubber foam padding between

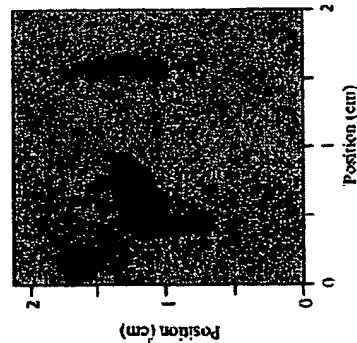


Fig. 10. THz transmission image of a portion  $\sim 2$  cm square of a small (1-3/8 oz.) box of cereal. The cardboard box in which the cereal is packaged is nearly transparent to the THz radiation. The dark areas in the image are raisins, which exhibit a high contrast relative to the surrounding material due to their high water content.

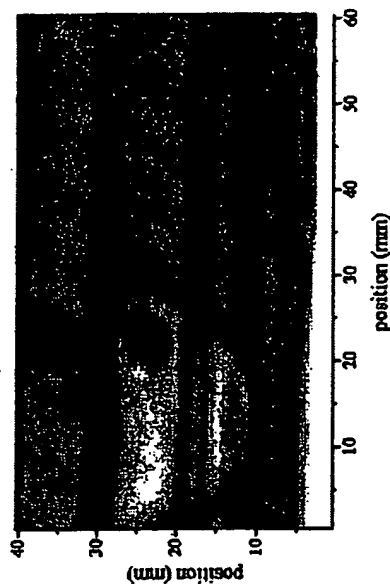


Fig. 11. THz transmission image of a portion of an automobile dashboard, showing a 1.5 cm diameter void in the foam padding between the two plastic surfaces. This type of manufacturing defect is very difficult to detect by any other means.

them. In the manufacturing process, the foam is sprayed between the plastic sheets, holding them together when it dries. However, occasionally bubbles or voids develop in the foam, sometimes as large as an inch in diameter or more. Detection of these voids is a significant quality control issue, and no simple method currently exists. X-ray transmission does not provide a high contrast between the plastic-rubber foam and the air; in addition, health and safety issues preclude the use of x-ray diagnostics here. Ultrasound analysis is effective only with the use of an index-matching fluid, while other probing techniques such as magnetic resonance imaging, are too expensive and cumbersome. Probing the parts with microwaves would work quite nicely, except that it would be difficult to detect voids significantly smaller than the wavelength of the radiation used. Since, in this case, it is desirable to detect voids smaller than one centimeter in diameter, this effectively eliminates conventional microwave analysis from consideration.

The THz imaging technique exploits the fact that the rubber foam filling has many tiny air pockets, which act as good scattering sites for radiation in the 0.5 mm wavelength range. The solid plastic surfaces on the front and rear of the sample are fairly transparent to the THz radiation. As shown in Fig. 11, the THz image clearly locates the void, identified as an increase in the transmission through the sample wherever a smaller length of foam is traversed. THz imaging is extremely sensitive to small voids or other morphological variations which may occur inside solid plastic or nonconducting composite parts. It may seem somewhat fortuitous that the foam rubber in this particular example consists of scattering sites ideally suited for the wavelength range spanned by the THz pulses. However, one should recall

that the THz radiation used in this imaging technique is extremely broadband, spanning more than one order of magnitude in wavelength. Further, it should be emphasized that one can detect voids of this sort without relying on such a coincidence by observing the *transit time* of the THz pulse through the material, rather than the transmitted *amplitude*. The combination of the amplitude and phase information measured in THz-TDS makes for a very powerful tool for quality control measurements.

Figure 12 illustrates this, showing two THz images of a chocolate bar. In the upper image, the grayscale is determined by the peak-to-peak amplitude of the THz pulse at each pixel, as in Figs. 10 and 11. The chocolate does not absorb much THz radiation, but several other features are visible. First, the sample has a plano-convex cross-sectional profile, and is therefore thinner at the top and bottom than in the middle. Second, the embossed letters are visible only because of scattering effects at their stepped edges, and as a result are rather difficult to read. Finally, because almonds absorb more THz radiation than chocolate, they can be easily detected using this technique; four almonds are visible in this image.

The lower image shows the same sample, but this image is formed using the *phase* of the transmitted THz pulse, rather than the amplitude, to encode the false-color scale at each pixel. As a crude measure of phase changes, one may simply monitor the change in the arrival time of the peak (or first zero

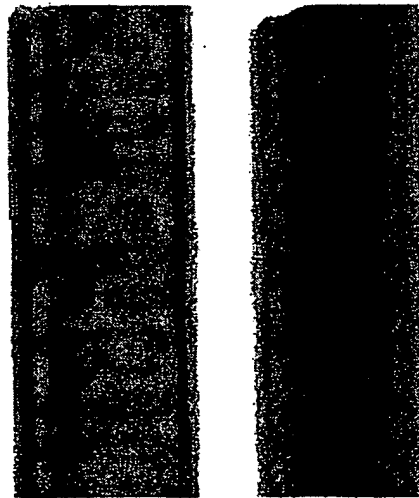


Fig. 12. THz images of a chocolate bar. In the upper image, the grayscale is determined by the peak-to-peak amplitude of the THz pulse at each pixel. The chocolate does not absorb much THz radiation, but several almonds are discernible. The lower image is encoded according to the travel time of the THz pulse through the image, which highlights variations in thickness more than changes in composition. Data courtesy of J.V. Rudd, Picometrix Inc.

crossing) of the THz waveform. Changes in this arrival time as a function of position on the sample indicate changes in the optical path length of the THz beam relative to the femtosecond beam which gates the receiver. This may result from either changes in the thickness of the sample as it is scanned transversely across the THz beam, or changes in the refractive index, or both. The change in arrival time  $\Delta t$  is given by  $\Delta t = (1/c) \int n(z) dz$ , where  $n(z)$  is the refractive index sampled by the THz beam along its optical path, and where the integral is taken along the path. In the lower part of Fig. 12, the sample is fairly homogeneous (except for the almonds), and so the phase delay image primarily contains information about the thickness of the sample at each point. Thus, the embossed letters and the overall thickness variation are much more prominent. The almonds are nearly invisible, except for the very dark regions where the transmitted pulse was too small for an accurate determination of the arrival time.

Figure 13 demonstrates one way in which the phase information contained in the THz waveforms can be used to form images which contain different information from those encoded on the basis of amplitude alone. Another example, which illustrates the impressive sensitivity of the technique to small changes in delay, is shown in Fig. 13, where a small gas flame has been imaged in transmission. In this experiment, the ionized molecules which make up the flame may have a significant absorption at certain frequencies within the spectrum of the pulse [9], but the gas density is so low that this effect cannot be observed. However, the flame heats the air locally, which changes the refractive index  $n(z)$  along the THz optical path. As a rough estimate of the magnitude of this effect, one may assume that the refractive index of

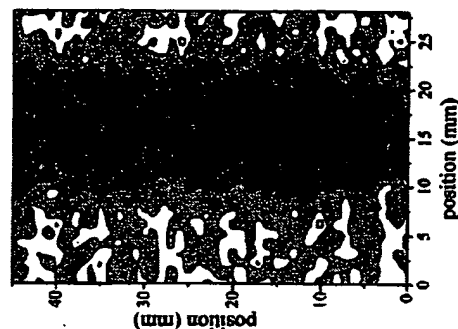


Fig. 13. THz image of a small gas flame. In which the grayscale is encoded according to the transit time of the THz pulse through the heated air. Adjacent contours correspond to shifts in transit time of only 5 fs

air varies inversely with temperature. If the flame has a thickness of roughly 5 mm, this would lead to a shift in the transit time of the THz pulse by  $\sim 3$  fs for a flame at 1000°C [68]. Each contour in Fig. 13 represents a shift of 5 fs in transit time. It is also worth noting that this and other THz-TDS measurements of flames [9] are unique for another reason. No other far-infrared detection system would be capable of performing these measurements, because the thermal emission from the sample would swamp the detector, and the much weaker probe beam would be nearly impossible to detect. Here, the gated detection and the averaging of incoherent fields combine to provide an impressive level of rejection for thermal radiation [14]. Not only does this permit spectroscopic measurements of flames, plasmas, or other thermally active samples, it also enables a host of interesting applications, such as in situ monitoring of sintering processes and engine exhaust testing.

These types of applications are not limited to quality control of consumer products. Figure 14 illustrates the use of THz imaging for the inspection of artwork. Figure 14a is a visible image of a piece of parchment, upon which an inscription has been written. The inscription has been painted over with a thick layer of black paint. The parchment was then imaged with T-rays, in an attempt to reveal the hidden writing. Because the black paint overlayer is not a leaf-based paint, it is transparent to THz radiation. Depending on the writing implement used to form the original inscription, the THz image may or may not show the underlying writing. Figure 14b shows a THz image of one sample, in which the original inscription ("OK") was written with a pencil. The thin graphite layer of the writing on the parchment provides sufficient amplitude contrast to be visible in the THz image. Not surprisingly, if the inscription is written with conventional ink, one cannot detect it in the THz image, because the dye molecules in the ink are nonpolar and thus do not absorb strongly in the THz range. This test suggests the possibility of using THz imaging for the investigation of underdrawings beneath paintings. This could be an excellent complementary technology to the mid-infrared and x-ray imaging systems currently used for such studies. More broadly,

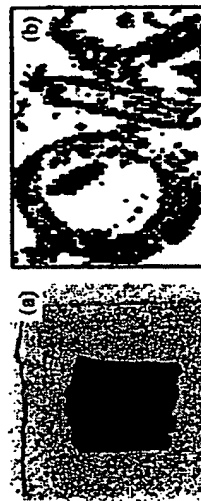


Fig. 14. (a) Visible and (b) THz images of a piece of paper on which some letters ("OK") have been written with a charcoal pencil, and then painted over with black latex paint. The paint layer is fairly transparent, but the graphite from the pencil provides sufficient contrast to form an image.

one can imagine that this new technique could be useful in a wide range of fields, including art history, archaeology, forensics, etc., in which one requires noninvasive methods for imaging. In this context, it is worth emphasizing that the power generated in the T-ray beam is extremely low, roughly 20–100 times less than the same power emitted from a room-temperature black body in the frequency range 0–3 THz. Thus, the risks to delicate or sensitive samples are minimal.

### 3.2 Terahertz Imaging of Liquid Water

The simplest type of image one can generate in a transmission imaging setup is one in which the transmitted power determines the nature of the image. A good example of this is shown in Fig. 15, which shows a THz transmission image of a leaf from a common houseplant. The color scale is determined by the amplitude of the transmitted THz power, which in turn is related to the amount of moisture present at each point on the leaf. (The dashed line across the figure refers to the measurements of Fig. 16, discussed below.) This image illustrates the extreme sensitivity of this technique to water content. In this frequency range, water absorbs quite strongly. Recently, a number of groups have used THz-TDS techniques to measure the properties of liquid water, in both transmission [69,70] and reflection [71] geometries. Typical values of  $\alpha \sim 230 \text{ cm}^{-1}$  at  $\nu \sim 1 \text{ THz}$  have been measured. This value has direct implications for the ultimate sensitivity of THz imaging to changes in water content. With a signal-to-noise ratio of 100:1 in the measured electric field, the minimum detectable water concentration is given by  $n\alpha \sim 10^{16} \text{ cm}^{-2}$ , where  $n$  is the density of water molecules and  $\alpha$  is the length of the path traversed by the THz beam in the material. In a material with a thickness of 1 mm, this implies a detection limit of less than  $10^{-6}$  of liquid density.

This extreme sensitivity to water content can be exploited in measurements such as those illustrated by Fig. 15. Indeed, this is of great interest as a method of measuring the water content of leaves on living plants. Currently, there is no accepted, nondestructive procedure for measuring the leaf

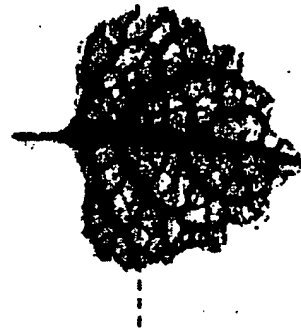


Fig. 15. THz transmission image of a living leaf from a common houseplant. This plant was water-starved for several days before this image, so the stems, containing most of the water, exhibit large contrast. The dashed line across the figure represents the location of the line scans shown in Fig. 16.



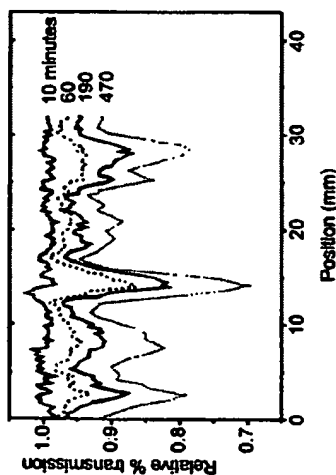


Fig. 16. Relative percentage transmission of the THz pulse through a living leaf, as a function of position along the dashed line in Fig. 15. The plant was water-starved for several days before these measurements, and watered at  $t = 0$ . Water uptake into the leaf is clearly observed, as the transmission drops steadily in the hours following the watering.

water status of a transpiring plant [72]. Research in the field of plant water relations has been limited to point-in-time observations that provide average values across the tissue being studied [73]. Multiple spatial and repeated temporal observations have been required to account for the dynamic movement of water through the plant and for spatial variation in water status in individual leaves. Using THz imaging, it is possible to account for inhomogeneities in the sample by performing a spatially resolved measurement. Because these measurements are inherently nondestructive, repeated measurements may be made on the same tissue, thereby providing for the study of water flow dynamics. A demonstration of this application is shown in Fig. 16, in which the percentage change in amplitude of the transmitted THz radiation (relative to the transmission immediately before watering) is shown as a function of horizontal position across a leaf, at various delay times after the plant was watered. The approximate location on the leaf of these line scans is shown by the dashed line in Fig. 15. In Fig. 16, the variations observed as a function of position on the leaf, which are repeated at each delay time, reflect the different transmission coefficients through different parts of the sample. These result primarily from the stem structure: as seen in Fig. 15, the region of the line scans intersects the primary or central stem, as well as a number of subsidiary stems on either side. As a function of time after watering, the transmission decreases by several percent, indicating that water is absorbed into the leaf on a timescale of hours. Also, it is clear that water is absorbed more rapidly in the stems than in other parts of the leaf. Experiments such as this can be used to understand the early warning signs of plant water stress, and may be valuable aids in irrigation management for a wide range

of crops. Recently, other far-infrared techniques have been used to validate the measurement of leaf water content using THz radiation [74], although in these experiments the spatial resolution of the images was limited by the shortest wavelength generated, approximately 0.6 mm.

### 3.3 Processing for Amplitude and Phase Imaging

All of the images shown in the preceding two subsections used fairly simple methods for extracting information from the measured waveforms. For phase or time delay imaging, it is a simple matter to extract the arrival time of the waveform at each pixel. For amplitude imaging, several methods are possible. One can simply use the peak-to-peak amplitude of the time-domain waveform, for a measure of bandwidth-averaged transmission. Alternatively, one may perform a fast Fourier transform on each waveform, and then integrate over any desired frequency band in order to retain some measure of spectral information. This method is of particular interest if high spatial resolution is desired. By integrating only over the high-frequency portion of the waveform, one obtains only the information corresponding to those frequency components. Since the focal-spot size is inversely proportional to the frequency, one can essentially tune the spatial resolution in software, without manipulating any optics [40].

### 3.4 Reflection Imaging

As noted, the extreme sensitivity to liquid water can be of substantial benefit in certain applications. Yet, it seems to precludes an entire area of imaging research, namely that of biomedical diagnostics. Because of the strong absorption of liquid water, the penetration depth into living tissue is only a few hundred microns, far too small for imaging of internal systems. However, a THz imaging system which operates in a reflection geometry could be useful for studies of surface or near-surface properties of a wide range of materials, including opaque objects such as humans. Further, because of the short coherence length of the THz radiation, the reflection geometry presents a number of new imaging possibilities, including that of THz tomography. For this reason, as well as for reasons of instrumental simplicity, it is expected that many of the aforementioned applications will eventually be implemented in a reflection geometry.

Figure 17 shows one possible implementation of a reflection geometry, in which the THz beam is focused at the sample, and is reflected at near-normal incidence [66,75]. One can imagine performing time-of-flight measurements in a reflection geometry similar to those described in the transmission experiment above. This is similar in principle to ultrasonic imaging. A commonly encountered problem in ultrasonic imaging is the large difference in acoustic impedance between air and liquid or solid objects, which necessitates some form of index matching. For terahertz waves, the dielectric constants of many

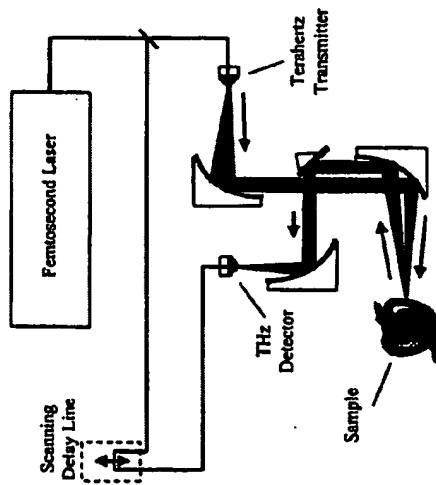


Fig. 17. Schematic of a reflection-mode THz imaging system

materials are not too different from that of air, and index matching is therefore not usually required.

THz time-of-flight imaging is also similar in certain respects to optical coherence tomography (OCT), in the sense that it is a reflection imaging technique which utilizes a broadband radiation source to achieve depth resolution. In OCT, a short-coherence-length optical source is split into two beams: one is reflected off the sample and the other off a reference. The two are then correlated to provide information about the reflectivity of the sample [76,77]. Distance measurements are possible because a correlation signal is only measured when the path length of the reference arm is equal to that of the sample arm, within the coherence length of the light source. As a result, the depth resolution is limited by the coherence length of the source.

As illustrated above, the THz measurement is not limited in the same way. The coherence length of a THz pulse is related to the pulse duration, which is on the order of several hundred femtoseconds. However, the measurement of the flame presented in Fig. 13 demonstrates a sensitivity to temporal shifts as small as 5 fs. This sensitivity stems from the phase-sensitive nature of the measurement, and from the fact that each THz pulse is a single cycle of the electromagnetic field. It is possible to measure the zero crossing of an electric field much more accurately than the peak of an intensity autocorrelation. Using this simple idea, it is possible to measure changes in either refractive index or thickness with extremely high accuracy. For example, one can detect, in transmission, a single sheet of paper added to a stack; in reflection, it is possible to achieve a depth resolution of a few microns. The limitation in this measurement is simply the accuracy with which the optical scanning delay line repeats its position on each scan. This is in contrast to the situation

where two reflecting surfaces are close to one another; in that case, the ability to distinguish these two surfaces is limited by the coherence length of the radiation in the intervening medium. For typical THz imaging systems, this length is on the order of a few hundred microns. It is possible to overcome this limit, through the use of interferometric techniques. This method, which can provide a dramatic enhancement in the detectability of thin or subtle features in an object, is described below.

### 3.5 Burn Diagnostics

As noted above, a possible use of THz reflection imaging is in the area of biomedical diagnostics, where the samples may consist of only one reflecting surface, but with a complex morphology. An example of an application in this area is the study of surface or near-surface skin properties, such as in the diagnosis of burn depth and severity. A reliable noninvasive probe of burn depth would be of great value to clinicians, who currently have no such technology. The application of optical probes to this problem has been an active research area recently [78]. More examples of biological and biomedical applications of THz imaging can be found in the chapter by Koch in this volume.

Figures 18–20 show the results of a simple experiment to illustrate the idea of burn diagnosis using THz pulses. This demonstration experiment used chicken breast as a model tissue system. The tissue was burned using an argon ion laser, producing a series of circular burns of increasing severity. Figure 18 shows a terahertz reflection image of one such burn; here, the reflected THz energy is displayed in grayscale, with the center of the burn reflecting the least. Figure 19 shows a series of waveforms obtained by translating the sample relative to the THz spot, in 250  $\mu\text{m}$  steps. The central waveform  $E_{\text{cent}}(t)$  (thick line) was reflected off of the center of the burn, while the waveforms at either end of the series ( $E_{\text{end1}}$  and  $E_{\text{end2}}$ ) originated from reflections off undamaged tissue on either side of the burn. The distortions imposed upon  $E_{\text{cent}}$  relative to  $E_{\text{end1}}$  and  $E_{\text{end2}}$  reflect the modifications in the THz optical properties of the tissue as a result of the burn.

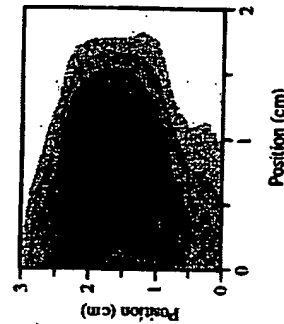


Fig. 18. THz reflection image of a burned region on a piece of chicken, used as a tissue phantom for these experiments. The burn was formed using the (circular) beam from an argon ion laser. The darker grayscale at the center of the burn indicates a decreased reflection of THz pulse energy

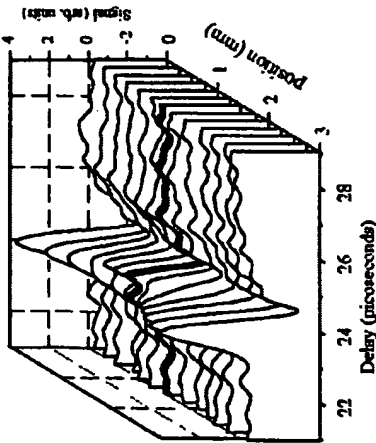


Fig. 19. A series of THz waveforms reflected from the burned region shown in Fig. 18, obtained by translating the sample across the THz beam spot in 0.25 mm steps. The waveform reflected from the center of the burn is the most distorted, and is highlighted

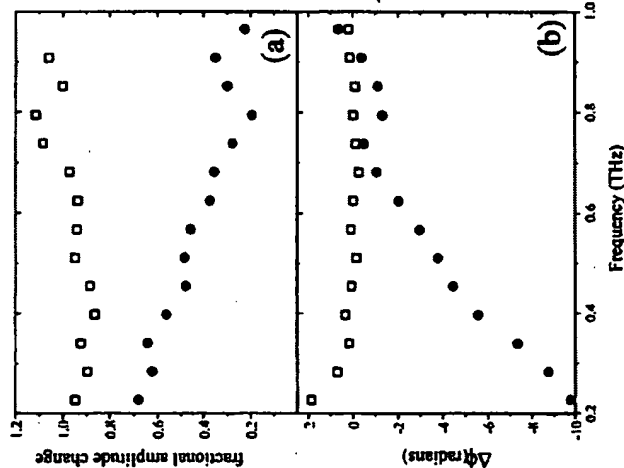


Fig. 20. (a) The open squares show the ratio of the spectral amplitudes of the two endmost waveforms in Fig. 19. This ratio is approximately unity, indicating that the unburned regions on either side of the burned tissue are nearly indistinguishable. The solid circles show the ratio of one of the endmost waveforms to the central waveform, showing the decreasing reflected amplitude at higher frequencies. (b) A comparison of the spectral phases of the two endmost waveforms (open squares), and of the endmost with the central waveform (solid circles)

We may analyze the waveform distortions by comparing  $E_{\text{refl}}$  with  $E_{\text{endl}}$  in the frequency domain. Figure 20 shows this comparison (solid circles) in both amplitude and phase. For reference, the two end waveforms are compared with each other as well (open squares). In Fig. 20a, it is clear that

$|E_{\text{refl}}/E_{\text{endl}}|$  is substantially less than one, and decreases with increasing frequency. This explains the relatively restricted bandwidth of this measurement; above 1 THz, the waveform reflected from the burn is attenuated to below the noise limit. Figure 20b shows that the relative phase of the two waveforms is also modified by the properties of the burned tissue, at least below 0.7 THz. The reasons for these modifications of  $n(\omega)$  and  $\alpha(\omega)$  remain unclear, although they cannot be attributed solely to changes in surface water content [71]. A number of chemical and morphological modifications occur when tissue is burned, and any one or a combination of several factors could be responsible. The fact that distinct, frequency-dependent effects are observable is an encouraging indication of the potential value of this technology.

### 3.6 Terahertz Tomography: The Third Dimension

For an object with multiple reflecting internal surfaces, the reflected waveform consists of a series of replicas of the input pulse of varying magnitude, polarity, and temporal distortion. This is illustrated here using the example of a 3.5 inch floppy disk. Typical waveforms are shown in Fig. 21. The upper waveform (Fig. 21a) was obtained by replacing the object with a mirror, and thus represents the pulse incident on the sample. The small oscillations which follow the main pulse in this waveform are a result of residual water vapor in the beam path [79], and do not affect the measurement significantly. The second curve (Fig. 21b), a representative reflected waveform, consists of a series of replicas of the input waveform. These correspond to reflections from the dielectric interfaces of the floppy disk, either from air to plastic, from plastic to air, or from the surfaces of the magnetic recording material. The polar-

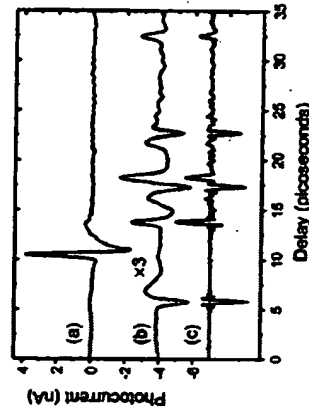


Fig. 21. THz waveforms (a) incident on, and (b) reflected from a conventional 3.5 inch floppy disk. Each buried dielectric interface within the disk generates a distinct reflected pulse, which can be discerned in (b). The waveform in (c) represents the Fourier deconvolution of the incident pulse shape (a) from the reflected waveform (b)

ity and magnitude of each reflection are given by the reflection coefficient at each interface, and are related to the size and sign of the corresponding index step. The four reflections resulting from the front and back plastic covers are clearly resolved. However, the thickness of the magnetic recording material is so small that the waveforms returned from its front and back surfaces cannot be distinguished, and appear as a single distorted waveform. In this example, the temporal waveforms hardly change shape while traversing the object because the plastic material has little absorption and dispersion. In a more general situation, reflected waveforms may be significantly altered in shape.

Figure 21c shows the waveform of Fig. 21b, after numerical Fourier deconvolution (i.e. division of the Fourier spectra of the incident and reflected waveforms, with a low-pass filter to remove noise above  $\sim 2.5$  THz). Subsequently, a low-frequency background was removed by wavelet filtering [80]. This procedure produces a sharp spike at a time delay corresponding to the position of every reflecting interface. Thus, the procedure helps to determine more accurately the positions of the various interfaces. In contrast to Fig. 21b, the front and back surfaces of the thin ( $\sim 120$   $\mu\text{m}$ ) magnetic recording material are clearly resolved in the deconvolved data. This is consistent with the expected resolution of  $L_c/2$ , where  $L_c = 200$   $\mu\text{m}$  is the coherence length of the THz pulse in the intervening material in this particular example.

Figure 22 shows a conventional T-ray image of a section of the floppy disk obtained in reflection. This image was obtained by computing the total reflected power, as described above. The plastic cover with its various features, the circular recording disk, and the metallic hub in the center of the disk can be distinguished. Figure 23 illustrates a tomographic T-ray "slice" of the floppy disk at a particular vertical position ( $y = 15$  mm) in Fig. 22. For each horizontal ( $x$ ) position, a reflected waveform was acquired, and displayed as a function of delay in this tomographic image. The upper image shows the resulting image using the raw waveforms, with no post-processing. The amplitude of the processed waveform has been translated into a grayscale, so that each reflecting surface appears as a pair of stripes, one for the positive

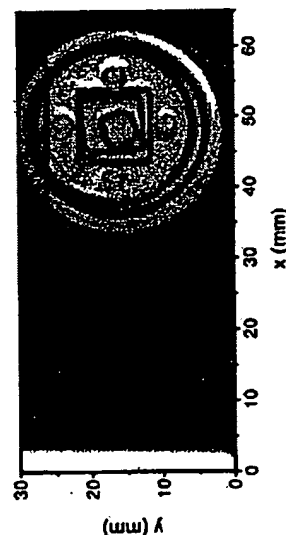


Fig. 22. A conventional THz reflection image of a portion of the floppy disk

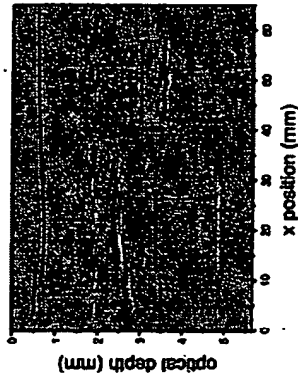
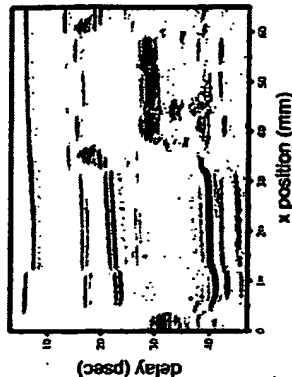


Fig. 23. A THz tomographic slice through the floppy disk, showing the depths of various buried interfaces. The upper image is formed using raw waveforms, with no post-processing. Since the THz pulses are approximately single cycles, each reflecting surface generates a double stripe in this image, one for the positive lobe and one for the negative lobe. The lower image shows the result after the waveforms are deconvolved as in Fig. 21c. The internal structures of the floppy disk are easily resolved

lobe of the THz waveform and one for the negative lobe. The lower image illustrates the improvements which result when each waveform is processed as described above (Fig. 21c) prior to forming the image. The positions of the various parts of the floppy disk along the propagation direction of the THz beam can be observed clearly in this image, such as the front and back cover, the magnetic recording disk, and the metal hub. The image also shows some artifacts of the technique resulting from multiple reflections between the various interfaces, such as the features observed behind the (opaque) metal hub, and the apparent discontinuity in the magnetic recording medium caused by a change in the thickness of the front plastic cover at  $x = 12$  mm.

### 3.7 Interferometric Tomography

In the image of the floppy disk, it is possible to resolve the front and rear surfaces of the thin recording material because they are separated by slightly more than one coherence length. In most tomographic imaging techniques, this is a strict bound on the achievable depth resolution. This limit can be understood most intuitively in the time domain: if the pulses used to distinguish between two closely spaced reflecting surfaces are broad compared with the temporal separation between them, then it becomes difficult to distinguish

them as two distinct pulses. For transform-limited pulses (those whose temporal duration is as short as can be achieved with the given bandwidth), this translates directly into a criterion in the frequency domain, which is precisely analogous to the well-known Rayleigh criterion for resolving two closely spaced light sources. Because the THz pulses used in these studies are quite broadband, a coherence length of a few hundred microns is easily achieved.

It is possible, however, to obtain images which far exceed the Rayleigh criterion in depth resolution with coherent radiation, through the use of interferometry [81]. Figure 24 shows a schematic of an interferometric imaging arrangement. This has a simple Michelson geometry, in which the reference arm mirror is mounted on a manual translation stage for varying the relative delay between the two arms of the interferometer. A focusing lens is inserted in the sample arm, to provide spatial resolution at the sample surface. This lens has a second crucial function, which enables the enhanced imaging capability. Because the pulse which is reflected off the sample surface has passed through a focus, it acquires a geometrical phase known as the Gouy phase shift [55], which is approximately equal to  $\pi$ . In contrast, the pulse which traverses the reference arm of the interferometer is not focused, and thus does not acquire any additional phase shift. As a result, if the sample is replaced by a metal mirror, these two pulses, otherwise identical, are nearly  $180^\circ$  out of phase when they interfere at the detector, and almost no signal is detected. This cancellation is disrupted if the pulse is distorted in any way during its interaction with a sample at the focus of the lens. Small distortions in either

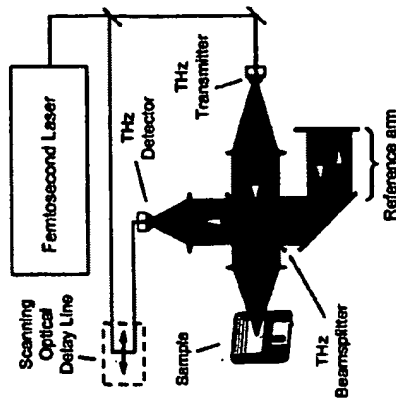


Fig. 24. A schematic of the apparatus used for interferometric tomography using THz pulses. The THz pulses are injected into a Michelson interferometer, with a lens in one arm. In addition to providing the lateral resolution for imaging, the lens also generates a phase shift of approximately  $\pi$  so that the pulses in the two arms of the interferometer can destructively interfere at the detector

amplitude or phase are thus converted into large changes in the measured signal amplitude.

Figure 25 shows typical waveforms which illustrate these effects. Curve (a) shows the waveform measured from the sample arm when the sample is simply a retroreflecting mirror, while (b) shows the waveform in the reference arm. Note that these two are nearly inverses of each other, denoting a relative phase shift of approximately  $\pi$ . Curve (c) shows the very small waveform which results when these two are allowed to interfere at the detector. This waveform is not precisely zero, because the Gouy phase shift is not precisely equal to  $\pi$  over the entire bandwidth of the THz pulse [55]. When a perturbation is introduced into the sample arm, such as by putting a thin ( $\sim 75 \mu\text{m}$ ) piece of tape across the retroreflecting mirror, the resulting waveform is dramatically altered, as shown in curve (d). The fractional change in the measured waveform upon introduction of this perturbation can be many times as large as the equivalent change observed without interferometry.

Figure 26 illustrates this enhancement in an imaging context [81]. In order to simulate thin air gaps between a metal and a dielectric material, a series of grooves of controlled depth were milled into a Teflon block. This block was pressed against a metal mirror, so that the focused THz beam

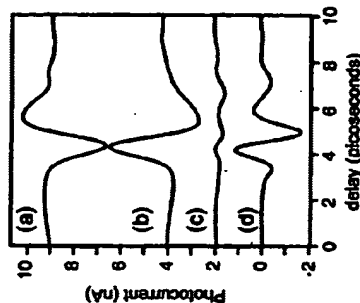


Fig. 25. (a) Waveform measured from the sample arm of the interferometer, with the reference arm blocked. (b) Waveform measured from the reference arm with the sample arm blocked. This is approximately  $\pi$  out of phase from the sample arm waveform shown in (a), owing to the Gouy phase shift. (c) The destructive interference of the waveforms in (a) and (b). The small residual signal results from the fact that the Gouy phase is not precisely equal to  $\pi$  at all frequencies. (d) When a thin piece of dielectric tape is placed on the mirror in the sample arm, the additional delay it introduces disrupts the destructive interference, leading to a large waveform which resembles the derivative of the waveform in (a). In this case, the thickness of the tape is roughly  $1/4$  of the coherence length of the THz pulses used to make the measurements

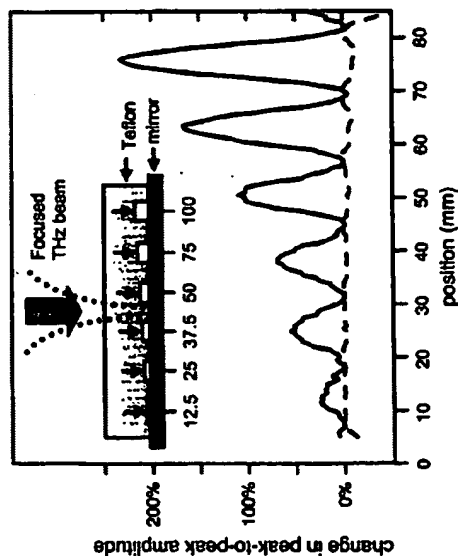


Fig. 26. The inset shows a schematic of the Teflon-metal composite sample, with air gaps of calibrated widths, fabricated for these measurements. The curves show the percentage change in peak-to-peak amplitude of a THz waveform reflected from this sample, relative to that of a waveform reflected from a position on the sample with no air gap. The dashed curve shows the result obtained with no interferometry, while the solid curve shows the enhanced contrast and sensitivity provided with the use of interferometry.

was incident through the back of the dielectric block, as shown schematically in the inset of Fig. 26. The numbers 12.5 through 100 indicate the depths of the grooves, in microns. This sample was scanned transverse to the THz beam direction, and a reflected waveform was collected every 500  $\mu\text{m}$ . The peak-to-peak amplitudes of these waveforms were then compared with the peak-to-peak amplitude of a waveform collected using a Teflon block with no grooves. The dashed curve shows this fractional change in contrast as a function of position along the line scan, without interferometry. Here, the 50  $\mu\text{m}$  and 100  $\mu\text{m}$  air gaps are discernable, but only barely. The solid line shows the equivalent measurement with interferometry. This demonstration shows an enormous increase in contrast for the detection of thin features, as well as a reasonable sensitivity to even the smallest (12.5  $\mu\text{m}$ ) gap. This gap is about 100 times smaller than the coherence length of the radiation used in this measurement, which was a relatively modest 1.1 mm.

#### 4 Future Prospects

One of the most exciting aspects of this field is the tremendous prospects for the future. It should be clear from the examples shown here that there are numerous potential "real-world" applications of THz imaging. In some cases, THz radiation may provide the only feasible option for certain tasks, whereas in others it might be only one of several competing technologies. It is clear that, in these latter cases, crucial factors in the successful implementation of systems of the kind described here include their cost and ease of use. These issues have historically been beyond the purview of research scientists, but modern research can no longer afford to ignore such practical concerns. In the case of THz imaging, much concerted effort has led to the development of a commercially available system based on photoconductive generation and detection techniques [20]. A photograph of the recently announced "T-Ray 2000" spectrometer is shown in Fig. 27. This system is reliable and easy to operate, and can be reconfigured for either transmission or reflection imaging. As of this writing, this system is already operating in one factory, as an on-line quality control monitor, with a number of other exciting prospects on the horizon.



Fig. 27. Photograph of the "T-Ray 2000", the first commercial THz time-domain spectrometer, manufactured by Picometrix, Inc

#### References

1. Y. R. Shen, "Far-Infrared generation by optical mixing", *Prog. Quantum Electron.* 4, 207 (1976).
2. P. R. Smith, D. H. Auston, M. C. Nuss, "Subpicosecond photoconductive dipole antennas", *IEEE J. Quantum Electron.* 24, 255 (1988).
3. Ch. Fattinger, D. Grischowsky, "Terahertz beams", *Appl. Phys. Lett.* 54, 480 (1989).

4. M. C. Nuss, J. Orenstein, "Terahertz time-domain spectroscopy", in *Millimeter and Submillimeter Wave Spectroscopy of Solids*, ed. by G. Gruner (Springer, Berlin, Heidelberg 1998).
5. H. Harde, S. Keiding, D. Grischkowsky, "THz commensurate echoes: periodic repheasing of molecular transitions in free-induction decay", *Phys. Rev. Lett.* **68**, 1834 (1991).
6. H. Harde, D. Grischkowsky, "Coherent transients excited by subpicosecond pulses of terahertz radiation", *J. Opt. Soc. Am. B* **8**, 1642 (1991).
7. H. Harde, N. Katzenellenbogen, D. Grischkowsky, "Terahertz coherent transients from methyl chloride vapor", *J. Opt. Soc. Am. B* **11**, 1018 (1994).
8. H. Harde, N. Katzenellenbogen, D. Grischkowsky, "Line-shape transition of collision broadened lines", *Phys. Rev. Lett.* **74**, 1307 (1995).
9. R. A. Cheville, D. Grischkowsky, "Far-infrared terahertz time-domain spectroscopy of flames", *Opt. Lett.* **20** (1995).
10. H. Harde, R. A. Cheville, D. Grischkowsky, "Collaboration-induced tunneling in methyl halides", *J. Opt. Soc. Am. B* **14**, 3282 (1997).
11. R. A. Cheville, D. Grischkowsky, "Far-infrared foreign and self-broadened rotational linewidths of high-temperature water vapor", *J. Opt. Soc. Am. B* **16**, 317 (1999).
12. B. B. Hu, M. C. Nuss, "Imaging with terahertz waves", *Opt. Lett.* **20**, 1716 (1995).
13. T. Clancy, S. Piecznik, *Games of State*, (Penguin Putnam, New York, 1990).
14. M. van Exter, D. Grischkowsky, "Characterization of an optoelectronic terahertz beam system", *IEEE Trans. Microwave Theory Tech.* **38**, 1684 (1990).
15. P. Jepsen, R. H. Jacobsen, S. R. Keiding, "Generation and detection of terahertz pulses from biased semiconductor antennas", *J. Opt. Soc. Am. B* **13**, 2424 (1996).
16. D. M. Mittleman, R. H. Jacobsen, M. C. Nuss, "T-ray imaging", *IEEE J. Sel. Top. Quantum Electron.* **2**, 679 (1996).
17. Q. Wu, T. D. Hewitt, X.-C. Zhang, "2-dimensional electro-optic imaging of THz beams", *Appl. Phys. Lett.* **69** (1996).
18. I. Brener, D. Dykaar, A. Frommer, L. N. Pfeiffer, J. Lopata, J. Wynn, K. West, M. C. Nuss, "Terahertz emission from electric field singularities in biased semiconductors", *Opt. Lett.* **21**, 1924 (1996).
19. Y. Cai, I. Brener, J. Lopata, J. Wynn, L. N. Pfeiffer, J. Federici, "Design and performance of singular electric field terahertz photoconducting antennas", *Appl. Phys. Lett.* **71**, 2076 (1997).
20. J. V. Rudd, D. Zimdars, M. Warmuth, "Compact, fiber-pigtailed terahertz imaging system", *Proc. SPIE* **3934**, 27 (2000).
21. R. Takahashi, Y. Kawamura, H. Iwanura, "Ultrafast 1.55  $\mu\text{m}$  all-optical switching using low-temperature-grown multiple quantum wells", *Appl. Phys. Lett.* **68**, 153 (1996).
22. L. Qian, S. D. Benjamin, P. W. E. Smith, B. J. Robinson, D. A. Thompson, "Picosecond carrier lifetime and large optical nonlinearities in InGaAsP grown by He-plasma-assisted molecular beam epitaxy", *Opt. Lett.* **22**, 108 (1997).
23. T. Kondo, M. Sakamoto, M. Tonouchi, M. Hangyo, "Terahertz radiation from (111) InAs surface using 1.55  $\mu\text{m}$  femtosecond laser pulses", *Jpn. J. Appl. Phys. Pt. 2 (Lett.)* **38**, 1035 (1999).
24. N. Sekine, K. Hirakawa, F. Sogawa, Y. Arakawa, N. Usami, Y. Shiraki, T. Katoda, "Ultrashort lifetime photocarriers in Ge thin films", *Appl. Phys. Lett.* **68**, 3419 (1996).
25. N. Katzenellenbogen, D. Grischkowsky, "Efficient generation of 380 fs pulses of THz radiation by ultrafast laser pulse excitation of a biased metal-semiconductor interface", *Appl. Phys. Lett.* **58**, 222 (1991).
26. S. E. Ralph, D. Grischkowsky, "THz spectroscopy and source characterization by optoelectronic interferometry", *Appl. Phys. Lett.* **60**, 1070 (1992).
27. M. Tani, S. Matsura, K. Sakai, S. Nakashima, "Emission characteristics of photoconductive antennas based on low-temperature-grown GaAs and semiconducting GaAs", *Appl. Opt.* **36**, 7853 (1997).
28. A. Bonvalet, M. Joffre, J.-L. Martin, A. Migus, "Generation of ultrabroadband femtosecond pulses in the mid-infrared by optical rectification of 15 fs light pulses at 100 MHz repetition rate", *Appl. Phys. Lett.* **67**, 2907 (1995).
29. Q. Wu, X.-C. Zhang, "7 terahertz broadband GaP electro-optic sensor", *Appl. Phys. Lett.* **70**, 1784 (1997).
30. Q. Wu, X.-C. Zhang, "Free-space electro-optic sampling of mid-infrared pulses", *Appl. Phys. Lett.* **71**, 1285 (1997).
31. F. G. Sun, G. A. Wagoner, X.-C. Zhang, "Measurement of free-space terahertz pulses via long-lifetime photoconductors", *Appl. Phys. Lett.* **67**, 1656 (1995).
32. J. Bromage, I. A. Walmsley, C. R. Stroud, "Dithered-edge sampling of terahertz pulses", *Appl. Phys. Lett.* **76**, 2181 (1999).
33. S. Gupta, M. Y. Frankel, J. A. Valdmanis, J. F. Whitaker, G. A. Mourou, F. W. Smith, A. R. Calawa, "Subpicosecond carrier lifetime in GaAs grown by molecular beam epitaxy at low temperatures", *Appl. Phys. Lett.* **59**, 3276 (1991).
34. F. E. Doany, D. Grischkowsky, G.-C. Chi, "Carrier lifetime versus ion-implantation dose in silicon on sapphire", *Appl. Phys. Lett.* **50**, 460 (1987).
35. Y. Cai, I. Brener, J. Lopata, J. Wynn, L. Pfeiffer, J. B. Stark, Q. Wu, X.-C. Zhang, J. F. Federici, "Coherent terahertz radiation: direct comparison between free-space electro-optic sampling and antenna detection", *Appl. Phys. Lett.* **73**, 444 (1998).
36. S. Kono, M. Tani, G. Ping, K. Sakai, "Detection of up to 20 THz with a low-temperature-grown GaAs photoconductive antenna gated with 15 fs light pulses", *Appl. Phys. Lett.* **77**, 4104 (2000).
37. D. Grischkowsky, S. Keiding, M. van Exter, C. Fattinger, "Far-infrared time-domain spectroscopy with terahertz beams of dielectrics and semiconductors", *J. Opt. Soc. Am. B* **7**, 2006 (1990).
38. P. Uhd Jepsen, S. R. Keiding, "Radiation patterns from lens-coupled terahertz antennas", *Opt. Lett.* **20**, 807 (1995).
39. R. W. McGowan, G. Gallot, D. Grischkowsky, "Propagation of ultrawideband short pulses of terahertz radiation through submillimeter-diameter circular waveguides", *Opt. Lett.* **24**, 1431 (1999).
40. S. Hunsche, M. Koch, I. Brener, M. C. Nuss, "THz near-field imaging", *Opt. Commun.* **150**, 22 (1998).
41. J. V. Rudd, D. M. Mittleman, "The influence of substrate lens design in terahertz time-domain spectroscopy", *J. Opt. Soc. Am. B* **19**, 319 (2002).
42. D. F. Filipovic, S. S. Gearhart, G. M. Rebeiz, "Double-dot antennas on extended hemispherical and elliptical silicon dielectric lenses", *IEEE Trans. Microwave Theory Tech.* **41**, 1738 (1993).

43. W. B. Dou, G. Zang, Z. L. Sun, "Pattern prediction of extended hemispherical lens/objective lens antenna system at millimeter wavelengths", *IEEE Proc. Microwave Antennas Propag.* **145**, 295 (1998).
44. J. R. Bray, L. Roy, "Performance trade-offs of substrate lens antennas," in Proceedings of the Symposium on Antenna Technology and Applied Electromagnetics (ANTEN), Ottawa, Canada, 1998, pp. 321-324.
45. M. N. Alsaar, "Precision millimeter-wave measurements of complex refractive index, complex dielectric permittivity, and loss tangent of common polymers", *IEEE Trans. Instrum. Meas.* **36**, 530 (1987).
46. J. R. Birch, "The far infrared optical constants of polyethylene", *Infrared. Phys.* **30**, 195 (1990).
47. K. Kawase, N. Hirokawa, "Terahertz-wave antireflection coating on Ge and GaAs with fused quartz", *Appl. Opt.* **37**, 1862 (1998).
48. C. R. Englert, M. Birk, H. Maurer, "Antireflection coated, wedged, single-crystal silicon aircraft window for the far-infrared", *IEEE Trans. Geosci. Remote Sens.* **37**, 1997 (1999).
49. J. R. Birch, E. A. Nicol, "The FIR optical constants of the polymer TPX", *Infrared Phys.* **24**, 573 (1984).
50. R. W. Ziolkowski, J. B. Juddkins, "Propagation characteristics of ultrawide-bandwidth pulsed Gaussian beams", *J. Opt. Soc. Am. A* **9**, 2021 (1992).
51. D. Yon, P. Buchsbaum, "Propagation of half-cycle far infrared pulses", *J. Opt. Soc. Am. B* **14**, 1651 (1997).
52. A. E. Kaplan, "Diffraction-induced transformation of near-cycle and subcycle pulses", *J. Opt. Soc. Am. B* **15**, 951 (1998).
53. P. Kuzel, M. A. Khazaei, J. Kroupa, "Spatiotemporal transformations of ultra-short terahertz pulses", *J. Opt. Soc. Am. B* **16**, 1795 (1999).
54. S. Hunsche, S. Feng, H. G. Winful, A. Leitenstorfer, M. C. Nuss, E. P. Ippen, "Spatiotemporal focusing of single-cycle light pulses", *J. Opt. Soc. Am. A* **16**, 2025 (1999).
55. A. B. Ruffin, J. V. Rudd, J. F. Whitaker, S. Feng, H. G. Winful, "Direct observation of the Gouy phase shift with single-cycle terahertz pulses", *Phys. Rev. Lett.* **83**, 3410 (1999).
56. J. Bronnagel, S. Radic, G. P. Agrawal, C. R. Stroud, P. M. Faudet, R. Sobolewski, "Spatiotemporal shaping of terahertz pulses", *Opt. Lett.* **22**, 627 (1997).
57. C. Winnewisser, F. Lewen, J. Weizier, H. Helm, "Transmission features of frequency-selective components in the far infrared determined by terahertz time-domain spectroscopy", *Appl. Opt.* **38**, 3961 (1999).
58. F. Garet, L. Duvallet, J.-L. Coutaz, "Evidence of frequency dependent THz beam polarization in time-domain spectroscopy", *Proc. SPIE* **3617**, 30 (1999).
59. J. V. Rudd, J. L. Johnson, D. M. Mittleman, "Quadrupole radiation from terahertz dipole antennas", *Opt. Lett.* **25**, 1556 (2000).
60. J. V. Rudd, J. L. Johnson, D. M. Mittleman, "Cross-polarized angular emission patterns from lens-coupled terahertz antennas", *J. Opt. Soc. Am. B* **18**, 1524 (2001).
61. A. J. Bahr, "Nondestructive evaluation of ceramics", *IEEE Trans. Microwave Theory Tech.* **26**, 676 (1978).
62. T. S. Hartwick, D. T. Hodges, D. H. Barker, F. B. Foote, "Far infrared imagery", *Appl. Opt.* **15**, 1019 (1976).
63. D. B. Rutledge, M. S. Muha, "Imaging antenna arrays", *IEEE Trans. Antennas Propag.* **30**, 535 (1982).
64. A. J. Cantor, P. K. Cheo, M. C. Foster, L. A. Newman, "Application of sub-millimeter wave lasers to high voltage cable inspection", *IEEE J. Quantum Electron.* **17**, 477 (1981).
65. P. K. Cheo, "Far-infrared lasers for power cable manufacturing", *IEEE Circuits Devices*, **2**, 49 (1996).
66. M. Bruchersleifer, P. Haring Bolivar, H. Klingenberg, H. Kurz, "Angle-dependent THz tomography characterization of thin ceramic oxide films for fuel cell applications", *Appl. Phys. B* **72**, 361 (2001).
67. D. M. Mittleman, J. Cunningham, M. C. Nuss, M. Geva, "Noncontact semiconductor wafer characterization with the terahertz Hall effect", *Appl. Phys. Lett.* **71**, 16 (1997).
68. J. C. Owens, "Optical refractive index of air: dependence on pressure, temperature and composition", *Appl. Opt.* **6**, 51 (1967).
69. J. T. Kindt, C. A. Schmittmaier, "Far-infrared dielectric properties of polar liquids probed by femtosecond terahertz pulse spectroscopy", *J. Phys. Chem.* **100**, 10373 (1996).
70. C. Renne, L. Thrane, P.-O. Åstrand, A. Wallqvist, K. V. Mikkelsen, S. R. Keiding, "Investigation of the temperature dependence of dielectric relaxation in liquid water by THz reflection spectroscopy and molecular dynamics simulation", *J. Chem. Phys.* **107**, 5319 (1997).
71. L. Thrane, R. H. Jacobsen, P. Uhd Jepsen, S. R. Keiding, "THz reflection spectroscopy of liquid water", *Chem. Phys. Lett.* **240**, 330 (1995).
72. P. F. Scholander, H. T. Hammett, E. D. Bradstreet, E. A. Hemmingsen, "Sap pressure in vascular plants", *Science* **148**, 339 (1965).
73. N. C. Turner, R. A. Spurway, E. D. Schulze, "Comparison of water potentials measured by in situ psychrometry and pressure chamber in morphologically different species", *Plant Physiol.* **74**, 316 (1984).
74. S. Hadjiloucas, L. S. Karatas, J. W. Bowen, "Measurements of leaf water content using terahertz radiation", *IEEE Trans. Microwave Theory Tech.* **47**, 142 (1999).
75. D. M. Mittleman, S. Hunsche, L. Boivin, M. C. Nuss, "T-ray tomography", *Opt. Lett.* **22**, 904 (1997).
76. D. Huang, E. A. Swanson, C. P. Lin, J. S. Schuman, W. G. Stinson, W. Chang, M. R. Hee, T. Flotte, K. Gregory, C. A. Pulaifto, J. G. Fujimoto, "Optical coherence tomography", *Science* **264**, 1178 (1991).
77. G. J. Tearney, M. E. Brezinski, J. F. Southern, B. E. Bouma, M. R. Hee, J. G. Fujimoto, "Determination of the refractive index of highly scattering human tissue by optical coherence tomography", *Opt. Lett.* **20**, 2258 (1995).
78. Z. B. Niaz, T. J. Essex, R. Papini, D. Scott, N. R. McLean, M. J. Black, "New laser doppler scanner, a valuable adjunct in burn depth assessment", *Burns* **19**, 485 (1993).
79. M. van Exter, C. Fattinger, D. Grischkowsky, "Terahertz time-domain spectroscopy of water vapor", *Opt. Lett.* **14**, 1128 (1989).
80. J. Buckheit, S. Chen, D. Donoho, I. Johnstone, J. Scargle, "Wavelab" software package, <http://playfair.stanford.edu/wavelab/> (1997).
81. J. L. Johnson, T. D. Dorney, D. M. Mittleman, "Enhanced depth resolution in terahertz imaging using phase-shift interferometry", *Appl. Phys. Lett.* **78**, 835 (2001).



**This Page is Inserted by IFW Indexing and Scanning  
Operations and is not part of the Official Record**

**BEST AVAILABLE IMAGES**

Defective images within this document are accurate representations of the original documents submitted by the applicant.

Defects in the images include but are not limited to the items checked:

- ☐ BLACK BORDERS
- ☒ IMAGE CUT OFF AT TOP, BOTTOM OR SIDES
- ☐ FADED TEXT OR DRAWING
- ☐ BLURRED OR ILLEGIBLE TEXT OR DRAWING
- ☐ SKEWED/SLANTED IMAGES
- ☐ COLOR OR BLACK AND WHITE PHOTOGRAPHS
- ☐ GRAY SCALE DOCUMENTS
- ☐ LINES OR MARKS ON ORIGINAL DOCUMENT
- ☒ REFERENCE(S) OR EXHIBIT(S) SUBMITTED ARE POOR QUALITY
- ☐ OTHER: \_\_\_\_\_

**IMAGES ARE BEST AVAILABLE COPY.**

**As rescanning these documents will not correct the image problems checked, please do not report these problems to the IFW Image Problem Mailbox.**